# Fine-grained high-performance $Ba_{0.85}Ca_{0.15}$ $Zr_{0.1}Ti_{0.9}O_3$ piezoceramics obtained by current-controlled flash sintering of nanopowders

Samuel López-Blanco [a], Diego A. Ochoa [a], Harvey Amorín [b], Alicia Castro [b], Miguel Algueró [b], Jose E. García [a,*]

[a] Department of Physics, Universitat Politècnica de Catalunya - BarcelonaTech, 08034 Barcelona, Spain
[b] Instituto de Ciencia de Materiales de Madrid (ICMM), CSIC, Cantoblanco, 28049 Madrid, Spain

## ARTICLE INFO

## ABSTRACT

Due to environmental concerns, extensive research has been carried out to develop high-performance lead-free piezoceramics capable of replacing commercial lead-based materials. The lead-free $(Ba_{0.7}Ca_{0.3})TiO_3 - Ba(Zr_{0.2}Ti_{0.8})O_3$ system has emerged as a candidate for room temperature transducer applications because a high piezoelectric charge coefficient is achieved in this system for compositions at the morphotropic phase boundary. However, conventional ceramic processing of these eco-friendly piezoceramics demands high energy consumption because long-lasting, high-temperature heat treatments are needed, which often lead to microstructural degradation that compromises the material reliability. Field-assisted flash sintering has started to be explored since the application of an adequate electric field was shown to significantly reduce the sintering time and temperature, thereby controlling grain growth. In this work, $Ba_{0.85}Ca_{0.15}Zr_{0.1}Ti_{0.9}O_3$ ceramics are obtained by current-controlled flash sintering of mechanosynthesized nanopowders. Exhaustive control of the sintering parameters allows tailoring of the microstructure, which allows dense fine-grained flash-sintered ceramics exhibiting a high electric field-induced strain response to be obtained.

## 1. Introduction

$BaTiO_3$-based piezoceramics, a family of lead-free perovskite structure piezoelectric materials, have attracted research interest worldwide because environmental regulations demand robust cyclic reliability for future piezoelectric technologies [1–3]. In this context, the $(Ba,Ca)(Zr,Ti)O_3$ system has emerged as a candidate for room temperature transducer applications since a high piezoelectric charge coefficient is achieved for compositions at the morphotropic phase boundary [4–6]. In particular, the $Ba_{0.85}Ca_{0.15}Zr_{0.1}Ti_{0.9}O_3$ compound (hereafter labeled BCZT) has received special attention because of its potential application as an active element for energy harvesting or bioimplanted transducers [7–9]. However, in addition to its rather low Curie temperature, an important drawback of BCZT is the difficult control of grain growth during conventional ceramic processing, thereby compromising reliability [10–12]. The required high sintering temperatures usually lead to abnormal grain growth (often shaping a bimodal microstructure) that results in a dramatic reduction in mechanical and electrical breakdown strengths, hindering BCZT transfer into applications [13,14].

Tailoring the microstructure toward sub10 μm-scale grain size is then desirable, but notable functionality degradation has been reported for fine-grained BCZT [15–17]. Therefore, novel synthesis and/or sintering methods for microstructure refinement are required to obtain high-performance BCZT ceramics with tailored microstructures. In this respect, nonconventional, faster-kinetic sintering routes requiring lower sintering temperatures and times should be explored. Flash sintering, for instance, is a novel field-assisted sintering route that is attracting growing interest because high-density ceramics can be obtained in a few minutes and at lower temperatures than those in conventional sintering [18–20]. In addition to the lower time and energy consumption, flash sintering also offers better grain growth control through proper selection of the electric current profile [21,22].

Although flash sintering has been used to obtain a wide variety of structural ceramics, its application for sintering electroceramics is still limited and is even scarce for piezoelectrics. Furthermore, works related to flash sintering of piezoceramics have been mainly focused on obtaining dense ceramics but have not paid true attention to tailoring the microstructure to enhance functional properties. In this work,

---

current-controlled flash sintering of highly reactive, mechanosynthesized nanopowders is used to obtain fine-grained BCZT with promising properties. Sintering parameters for obtaining sub10 μm-grain sized ceramics are established, and the functional properties are characterized. The results show that high-density BCZT ceramics with a homogeneous 2 μm grain size can be obtained by current-controlled flash sintering at moderate temperature and in a few minutes. Flash sintered BCZT ceramics exhibit good ferroelectric, piezoelectric and electromechanical properties.

## 2. Experimental procedure

### 2.1. Sintering experiments

Perovskite $Ba_{0.85}Ca_{0.15}Zr_{0.1}Ti_{0.9}O_3$ nanocrystalline powders were obtained by mechanosynthesis from stoichiometric mixtures of analytical grade $BaO_2$ (Fluka, $\geq$ 95% peroxide basis), $TiO_2$ (Cerac, 99.9% pure anatase), $CaTiO_3$ and $BaZrO_3$ (both Alfa Aesar, 99% metals basis) using tungsten carbide milling media in a high-energy planetary mill (Fritsch Pulverizette 6). Milling conditions were tailored to produce 10 g of nanopowder after 12 h of milling. The mechanosynthesized powder consisted of nanosized crystals with an average size of ~15 nm, exhibiting nanometer-scale chemical homogeneity. More details of the synthesis procedures and powder properties can be found elsewhere [12].

The mechanosynthesized single-phase nanocrystalline powder was then uniaxially pressed at 270 MPa to form the dog-bone shaped (supplementary Fig. S1a) green sample. A typical flash sintering setup (supplementary Fig. S1b) was employed, where the sample was placed in the furnace center hanging by its handles from two platinum electrodes. Platinum paint was used to ensure good electrical contact between the sample and the electrodes. Electrical contacts were adequately painted so that a uniform current flowed along the sample. A CCD camera was used for monitoring the sample shrinkage during the flash event.

In a conventional flash sintering experiment, the power supply works initially in voltage control mode, holding the sample at a constant electric field with a ramping furnace temperature. For materials with a negative temperature coefficient, the conductivity increases with temperature, and as a consequence, the electric current flowing through the sample slowly rises until an avalanche-like process occurs [18]. The power supply then changes to current control mode, maintaining a constant current to avoid overflow. In this work, flash sintering was carried out by using a current-controlled flash sintering (CCFS) setup, which was demonstrated to improve both density and microstructure homogeneity and has been shown to be an optimal approach for controlling grain growth [22–24]. In a CCFS experiment, the power supply works exclusively in current control mode while an adequate working temperature is maintained.

Samples were heated at a rate of 10 °C/min from room temperature until reaching the sintering temperature, which ranged from 1050 °C to 1200 °C depending on the experiment. The samples were then held in current control exclusively imposing a ramp-like current profile until the preset current limit was achieved. Finally, the samples were left to dwell until reaching the maximum current for 5 min (Supplementary Fig. S2). Conventional sintering (CS) was also carried out at 1450 °C for 4 h to obtain a control sample for comparison purposes [12]. The conventional sintered sample exhibited high densification (95% of the theoretical density) and a typical bimodal microstructure containing abnormally grown grains separated by regions of smaller grains. The average grain sizes for the two populations of grains are 8.5 μm and 28 μm. The microstructure, dielectric response, and ferroelectric hysteresis loop showed the expected behavior (Supplementary Fig. S3).

### 2.2. Microstructure and functional properties

Flash-sintered, dog bone shaped specimens were cut into 10 mm × 3 mm × 1 mm samples to avoid density inhomogeneities, which could be a critical issue in the vicinity of the electric contacts. Density was measured using a typical Archimedes setup. After that, samples were polished and then chemically etched for 1 min. The microstructure was assessed by using a field-emission scanning electron microscope (JEOL, JSM-7001 F). The average grain size was determined from SEM images by taking a statistically ample grain population. X-ray diffraction patterns of the most representative samples were obtained by using synchrotron radiation at beamline BM25 of the ESRF. A high flux monochromatic beam with a wavelength of 0.495 Å (~25 keV) was provided for measurement in transmission mode. The data were collected by using a high-resolution six-circle diffractometer.

Samples were then gold sputter coated on their parallel faces to ensure electrical contact for electrical characterization. An LCR meter (Agilent E4980A) was used to measure permittivity data of unpoled samples at various frequencies, ranging from 1 kHz to 1 MHz. Samples were placed in a closed-loop cryogenic system for ranging the temperature from 20 K up to 390 K. Electric field-induced polarization (*P-E*) hysteresis loops were measured in a typical Sawyer-Tower configuration by applying a triangular electric field with an amplitude of 2 kV mm$^{-1}$ at a frequency of 1 Hz and at room temperature. Unipolar electric field-induced strain (*S—E*) curves were obtained by using a WayCon inductive position transducer. Voltage was applied by a combination of a signal generator (Agilent 33120 A) and a power signal amplifier (Trek 663).

The nonlinear dielectric response of selected samples was evaluated at room temperature by measuring the variation in the real and imaginary parts of the permittivity with the variation in amplitude of the applied subswitching ac electric field at 1 kHz. A capacitance comparator bridge specially designed for this type of measurement was used to perform the characterization [25]. Samples were then poled at 4 kV mm$^{-1}$ for 20 min in a silicone bath at room temperature and subsequently aged for 24 h before further measurements to avoid the influence of the aging process. A $d_{33}$-meter (KCF Technologies, PM3500) was used to determine the static longitudinal direct piezoelectric coefficient.

## 3. Results and discussion

### 3.1. Current-controlled flash sintering

A comprehensive study on how flash sintering parameters influence the $BaTiO_3$ (BTO) microstructure has been recently published [22]. Since BCZT is a modification of BTO, flash conditions that allowed us to obtain dense BTO ceramics are used as starting points for this work. Conventional flash sintering experiments were performed under different electrical conditions (Supplementary Fig. S4), showing that a low electric field and/or high current density are required to obtain dense BCZT. Taking into account that there exists an inverse relation between the applied electric field and the temperature at which the flash event takes place [19,20], relatively high furnace temperatures are needed to make a useful CCFS experiment. For low furnace temperatures, the electric field that the power supply has to provide for maintaining the current flow is very high, and thus, low densities are achieved (Supplementary Fig. S4).

To probe the effect of current density on the CCFS of BCZT, an initial experiment was carried out at different maximum current values while the furnace temperature was maintained at 1200 °C. A second experiment was then performed at different furnace temperatures using the current density that previously yielded the best densification. The results show a direct relation between density and electrical current, except for the highest current (100 mA/mm$^2$) for which the sample broke due to the common damage that appears in high current flash events. Flash sintered samples are known to suffer electrochemical blackening and high reduction near the anode, leading to mechanically fragile specimens, as has been reported for several materials [20,22,26]. The evolution of electrical parameters measured during CCFS is

recorded in Fig. 1. Higher densities are achieved with increasing furnace temperature, which in turn yields a lower necessary electric field, as expected [20,22,26] (a full characterization of the electrical parameters during sintering can be found in Supplementary Fig. S5). The density values and the corresponding grain sizes are displayed in Table 1. As shown, fine-grained highly dense BCZT ceramics can be obtained by CCFS at a temperature 200 °C lower than that of conventional sintering and in a few minutes.

Regarding the microstructure, representative SEM images are shown in Fig. 2. A direct relation between average grain size and both maximum current density and furnace temperature seems to be clear. The grain size distribution becomes broader with increasing current density, while it stays reasonably constant with increasing furnace temperature, as shown in Supplementary Fig. S6. A high current density seems to be critical for a less homogeneous microstructure, which could be related to local heating or the percolative nature of flash sintering [20,26]. More detailed pore density information is found in Supplementary Fig. S7, where a distinction can be made between the two aforementioned sintering experiments. On the one hand, for constant furnace temperature experiments, increasing current correlates with the extinction of intragrain pores but at the cost of producing intergrain pores. This fact can be explained in terms of hotspot formation and localized overheating at grain boundaries [20], which correlates to the low density and fragility obtained for the sample sintered at 100 mA/mm². On the other hand, for constant current experiments, increasing the furnace temperature reduces both the size and density of the two pore types, which is similar to the expected behavior of a conventional sintering experiment at different temperatures.

Employing the video footage obtained with the CCD camera, the

**Table 1**

Sample density ($\rho$) and average grain sizes (Ø) obtained in controlled current flash sintering experiments carried out using different electric current densities and furnace temperatures. The dwell time was maintained at 5 min.

| T = 1200 °C | | | $J = 70$ mA/mm² | | |
|---|---|---|---|---|---|
| J (mA/mm²) | $\rho$ (%) | Ø (µm) | T (°C) | $\rho$ (%) | Ø (µm) |
| 30 | 93,9 | 0,90 ± 0,38 | 1050 | 94,6 | 1,30 ± 0,85 |
| 50 | 97,7 | 2,23 ± 0,90 | 1100 | 97,0 | 1,88 ± 0,98 |
| 70 | 99,1 | 2,15 ± 0,91 | 1150 | 97,6 | 1,95 ± 0,79 |
| 100 | 81,5 | 3,1 ± 1,2 | 1200 | 99,1 | 2,15 ± 0,91 |

difference between both sets of sintering experiments can be further studied by recoding the shrinkage evolution of the samples. Supplementary Fig. S8 gathers a shrinkage evolution comparison as a function of the most representative sintering parameters (i.e., sintering time, current density and applied electric power) for both sintering experiments. Two clear dissimilarities can be made again. On the one hand, for constant furnace temperature experiments, samples undergo a similar shrinkage evolution regardless of the maximum current density. In fact, shrinkage becomes stagnant for all cases upon reaching approximately 50 mA/mm². However, the samples end up having different densities, indicating that this stagnation may correspond to a change in the densification regime from intragrain densification to intergrain densification and localized melting if a high current is reached. Optimal densification for these experiments may be reached by employing lower current densities at lower rates. On the other hand, for the case of constant current experiments, samples undergo different shrinkage evolution during sintering. In fact, some samples do not become stagnant, indicating that the furnace temperature, and therefore the electric field, has a nontrivial effect on the densification dynamics. An appropriate set of furnace temperature, current density and current rate is therefore crucial to achieve a fine-tailored microstructure. It must be noted that the shrinkage data reported in Supplementary Fig. S8 should be taken carefully since the video footage is contaminated with temperature fluctuations. The purpose of these data is to show a qualitative comparison of shrinkage regimes and their change relation to sintering parameters. For a quantitative analysis of the obtained density, the Archimedes method is preferred, as reported in Table 1.

### 3.2. Functional characterization

Although fine-grained BCZT ceramics are desirable because of the improvement in the mechanical properties and dielectric strength, the overall material performance will depend on how functional properties change with grain size reduction. Hence, the dielectric, ferroelectric and electromechanical responses of CCFS samples are evaluated and compared with those of the CS sample. Fig. 3 shows the temperature dependences of the real (Fig. 3a) and imaginary (Fig. 3b) parts of dielectric permittivity for the higher density samples. The CCF sintered samples display a broader permittivity peak than the CS sample. Furthermore, the temperature of the maximum permittivity is lower in the CCF sintered samples than in the CS counterpart. The crystallographic transitions detected in the dielectric response of coarse-grained BCZT seem to merge into a single event for the fine-grained ones, which is a common feature of grain size downscaling of BCZT ceramics [16,27]. No evident relaxor behavior is evidenced from the frequency dependences of the dielectric response of the CCF sintered samples (Supplementary Fig. S9).

The ferroelectric character of the samples is evidenced in Fig. 4a, thereby revealing that the ferroelectric to paraelectric phase transition occurs above room temperature for all samples. Some differences in the ferroelectric response are found between the CCFS and CS samples, particularly the drop in the remnant polarization values, which may be related to differences in lattice distortion, as discussed below. The electric field-induced strain is displayed in Fig. 4b. A good
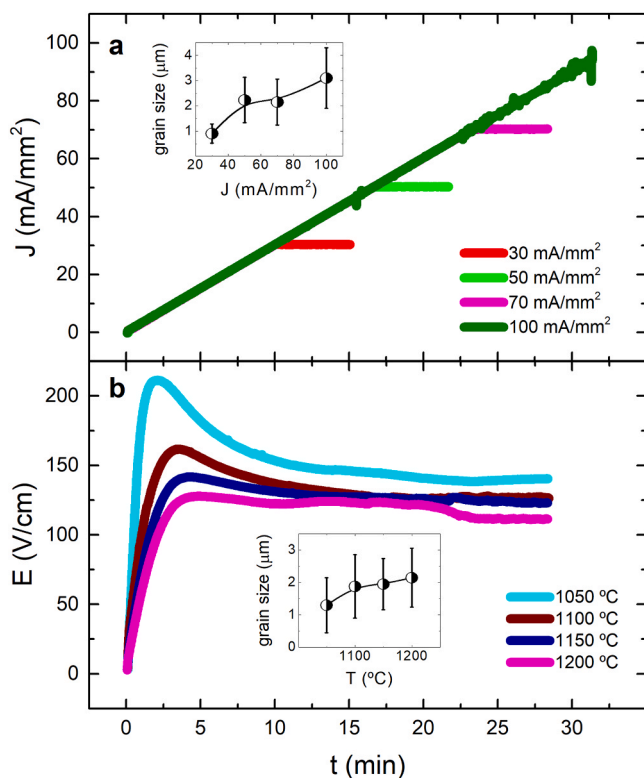


**Fig. 1.** Evolution of electrical parameters of CCFS experiments. (a) Current density profile and grain size of samples sintered at different maximum electric current densities. Furnace is held at 1200 °C for all cases. (b) Electric field profile and grain size of samples sintered under different furnace temperatures. The current density was maintained at 70 mA/mm². In both experiments, samples are left to dwell for 5 min after reaching their respective maximum current.
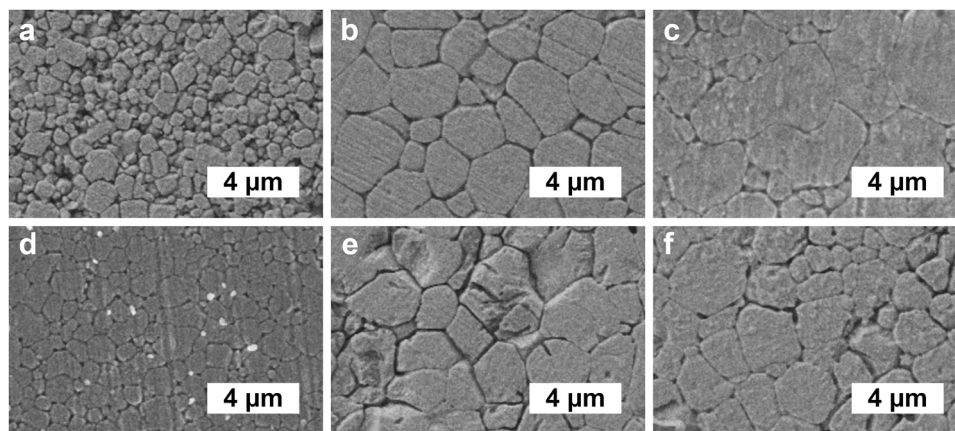
**Fig. 2.** Microstructure of the sintered samples. SEM images of BCZT samples sintered under different thermal and electrical conditions: (a) 30 mA/mm², 1200 °C; (b) 50 mA/mm², 1200 °C; (c) 70 mA/mm², 1200 °C; (d) 70 mA/mm², 1050 °C; (e) 70 mA/mm², 1100 °C; (f) 70 mA/mm², 1150 °C. The dwell time was 5 min for all cases.
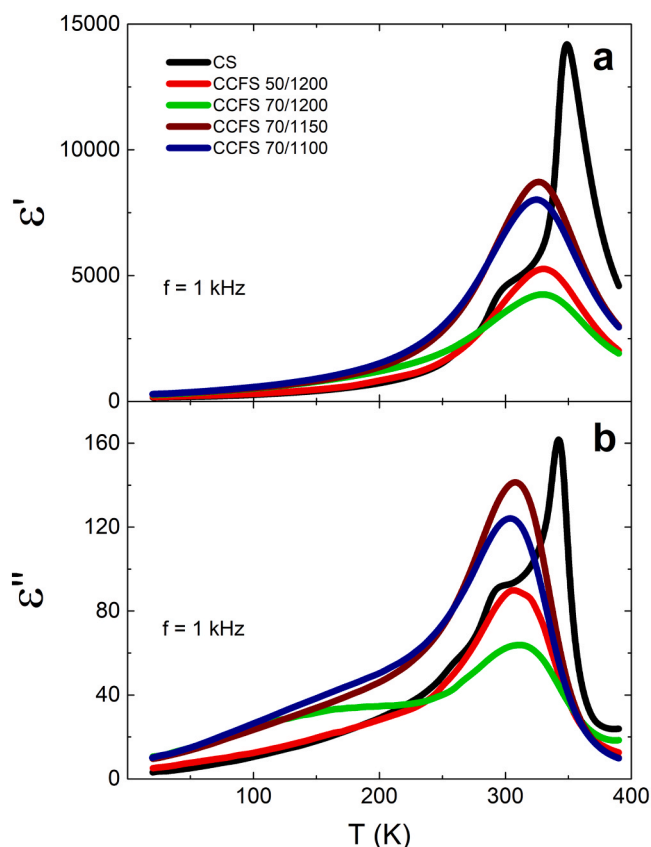


**Fig. 3.** Dielectric response of representative BCZT samples obtained by CCFS. Temperature dependence of the (a) real and (b) imaginary permittivity of samples sintered under different conditions, measured at 1 kHz. The dielectric response of the conventional sintered sample is also plotted for comparison.

electromechanical response is obtained for fine-grained CCF sintered BCZT with particular flash sintering conditions, i.e., for a relatively high current density and moderate furnace temperature. Values for some dielectric, ferroelectric and electromechanical properties of CCF-sintered BCZT are shown in Table 2, showing that fine-grained CCF-sintered BCZT can show promising functional properties. Better properties are obtained for dense samples sintered at lower temperatures (70/1100 and 70/1150), which could be explained in terms of the lower concentration of point defects. It is well known that higher sintering furnace temperatures lead to a higher concentration of point defects

such that the domain wall pinning effect becomes more relevant, leading to a drop in piezoelectric properties [28].

Synchrotron X-ray diffraction (SXRD) patterns of CCFS BCZT samples showing high electric field-induced strain (i.e., samples 70/1150 and 70/1100) were measured. Additionally, CS BCZT was also measured for comparison purposes. Fig. 5 displays three of the most significant reflections showing that the coarse-grained sample exhibits phase coexistence. The 222 reflection shows an asymmetry that does not correspond to a single tetragonal phase. In addition, the 400 and 440 reflections show a distribution of intensities that correspond better to a mix of phases than to a single tetragonal phase. SXRD results lead to the assumption that coarse-grained BCZT exhibits a polymorphic phase boundary, which occurs between the orthorhombic Amm2 and tetragonal P4mm phases [29–31]. Meanwhile, for the CCFS samples, the reflections clearly show a pseudocubic phase at room temperature. This crystallographic signature can explain the behavior of permittivity, where successive transitions merge into a single transition, and seems to indicate that tetragonal polymorphs are not present. However, the SXRD results cannot explain the high field-induced strain shown in Fig. 4b for these samples, leading to the consideration that other mechanisms, such as electric-field-induced phase transformation, could be present [32].

To shed light on the possible origin of the high field-induced strain response of fine-grained BCZT, the nonlinear dielectric behavior was evaluated. The nonlinear dielectric response of coarse-grained BCZT has been reported in a recent work [33]. The results, in the framework of the Rayleigh model, showed that the functional response of this material is mainly due to irreversible motion of ferroelastic domain walls, as previously evidenced [34]. Rayleigh law predicts that a relation between the increments of real and imaginary permittivity exists, such that an increment in the dielectric constant necessarily involves a certain increment in the dielectric losses. The model assumes that the nonlinear behavior is related to the irreversible motion of the domain walls in a random pinning center field [35], giving to the relation $\Delta\varepsilon''/\Delta\varepsilon' = 0.42$ [36].

Fig. 6 shows the real permittivity increment as a function of the applied electric field amplitude for the same samples that are studied by SXRD. On the one hand, the coarse-grained BCZT sample exhibits a large nonlinear response, i.e., a large variation in the dielectric permittivity, as expected [33]. Furthermore, the relation $\Delta\varepsilon''/\Delta\varepsilon'$ fulfills the Rayleigh law, thereby indicating that the major contribution to the nonlinear response in coarse-grained BCZT is the irreversible motion of domain walls [36,37]. In the context of the Rayleigh model, other extrinsic effects are not taken into account since the amplitude of the applied electric field is significantly lower than that of the coercive field [35].

Fine-grained BCZT samples, on the other hand, display a significantly lower nonlinear response, which could be expected by grain size
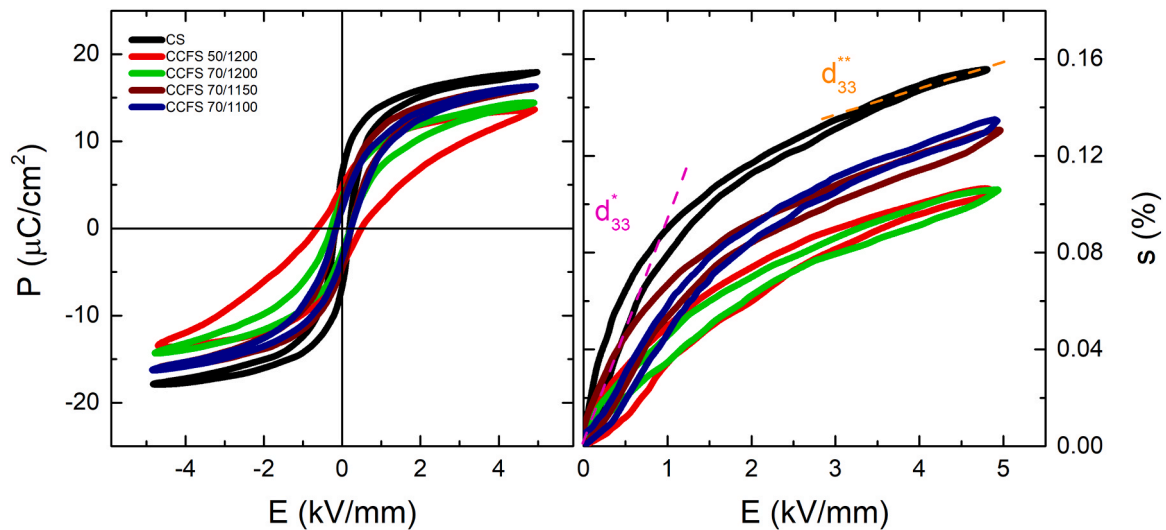
**Fig. 4.** Ferroelectric and electromechanical responses of representative BCZT samples obtained by CCFS. (a) Polarization-electric field (P-E) hysteresis loops and (b) field-induced strain of samples sintered under different CCF conditions, measured at 1 Hz and at room temperature.
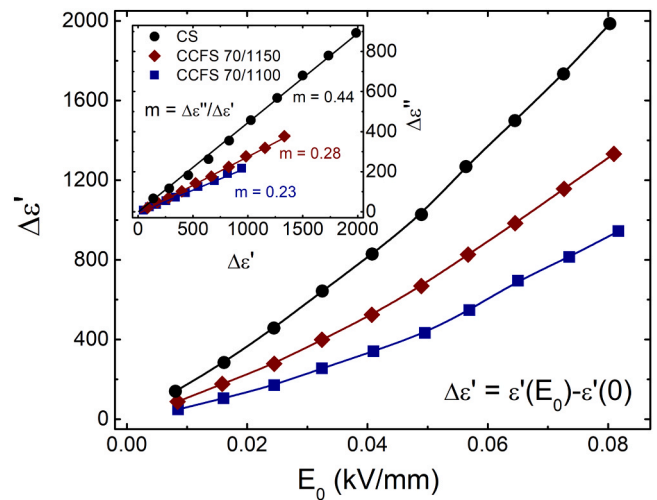
**Table 2**
Values of the room temperature dielectric constant ($\varepsilon$') and dielectric loss tangent (tan $\delta$), uniaxial piezoelectric constant ($d_{33}$), effective piezoelectric coefficient (Fig. 4b) in the low electric field region ($d^*$), effective piezoelectric coefficient in the high field linear region ($d^{**}$), maximum strain at 5 kV mm$^{-1}$ ($s_{max}$), remnant polarization ($P_r$), saturation polarization ($P_s$), and coercive field ($E_c$) of the most significant samples. Sample labels correspond to conventional sintering (CS); CCFS 70 mA/mm$^2$, 1200 °C (70/1200); CCFS, 70 mA/mm$^2$, 1150 °C (70/1150); CCFS, 70 mA/mm$^2$, 1100 °C (70/1100); CCFS, 50 mA/mm$^2$, 1200 °C (50/1200).

| Sample | $\varepsilon$' | tan $\delta$ (%) | $d_{33}$ (pC/N) | $d^*$ (pC/N) | $d^{**}$ (pC/N) | $s_{max}$ (%) | $P_r$ ($\mu$C/cm$^2$) | $P_s$ ($\mu$C/cm$^2$) | $E_c$ (kV/mm) |
|---|---|---|---|---|---|---|---|---|---|
| CS | 5110 | 1.99 | 390 | 750 | 150 | 0.159 | 7.0 | 18.2 | 0.19 |
| 70/1200 | 5500 | 1.42 | 105 | 380 | 125 | 0.083 | 3.2 | 14.5 | 0.22 |
| 70/1150 | 6880 | 1.53 | 140 | 470 | 180 | 0.136 | 3.9 | 16.4 | 0.21 |
| 70/1100 | 7470 | 1.47 | 145 | 450 | 160 | 0.137 | 3.1 | 16.4 | 0.17 |
| 50/1200 | 3290 | 2.06 | 100 | 370 | 140 | 0.085 | 6.2 | 13.7 | 0.55 |
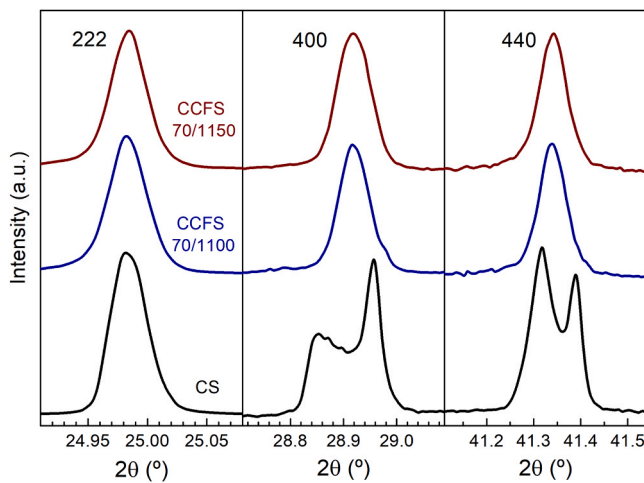


**Fig. 5.** Representative synchrotron X-ray diffraction peaks of selected BCZT samples. The 222, 400 and 440 reflections are plotted for the coarse-grained sample and for the fine-grained CCFS 70/1100 and 70/1150 samples.



**Fig. 6.** Nonlinear dielectric response of representative BCZT samples. Increase in the real relative permittivity, $\Delta\varepsilon$', as a function of the applied ac electric field amplitude for the CS coarse-grained sample and for the fine-grained CCFS 70/1100 and 70/1150 samples, measured at 1 kHz and at room temperature. Inset displays the relation between the increments of the real and imaginary permittivity, where values of $\Delta\varepsilon$''/$\Delta\varepsilon$' are also shown.

reduction, as reported for soft PZT [38]. A drastic decrease in the domain wall contribution should lead to a dramatic drop in the field-induced strain. However, this is not observed for these samples (Fig. 4b); therefore, another mechanism seems to contribute to the functional response of the CCFS BCZT. The values of the relation $\Delta\varepsilon$''/$\Delta\varepsilon$' for fine-grained samples are significantly lower than the value predicted by the Rayleigh model, suggesting that an additional contribution to the real permittivity exists. That is, an intrinsic contribution plays a crucial role in the functional response of fine-grained BCZT. The

combination of the results obtained from SRDX and the nonlinear response rule out the irreversible movement of domain walls as the origin of the high strain response, while suggesting that other intrinsic mechanisms, such as field-induced phase transformation, play an important role in the functional response of these materials.

## 4. Conclusion

Highly dense fine-grained $Ba_{0.85}Ca_{0.15}Zr_{0.1}Ti_{0.9}O_3$ ceramics are obtained by current-controlled flash sintering of nanopowders. Adequate electric current control of the flash sintering event allows a refined microstructure with a grain size of $\sim$2 μm to be obtained at furnace temperatures lower than 1200 °C (i.e., 300 °C lower than conventional sintering). Grain size effect features are observed in some functional properties of fine-grained samples, such as a broad temperature-dependent permittivity, moderate piezoelectric charge coefficient after poling, and reduced remnant polarization. However, an improved dielectric response and significant field-induced strain are obtained at room temperature. A basic crystallographic study shows that fine-grained materials exhibit a pseudocubic phase while showing unequivocal ferroelectric character, which indicates a drastic refinement of the domain configurations. Analysis of the nonlinear dielectric response in the framework of the Rayleigh law shows that an intrinsic mechanism might play a relevant role in the high strain under the electric field response achieved.

## Declaration of Competing Interest

The authors declare that they have no known competing financial interests or personal relationships that could have appeared to influence the work reported in this paper.

## Appendix A. Supporting information

Supplementary data associated with this article can be found in the online version at doi:10.1016/j.jeurceramsoc.2023.08.012.

## References

[1] M. Acosta, N. Novak, V. Rojas, S. Patel, R. Vaish, J. Koruza, G.A. Rossetti, J. Rödel, BaTiO3-based piezoelectrics: fundamentals, current status, and perspectives, Appl. Phys. Rev. 4 (2017), 041305.

[2] J. Gao, D. Xue, W. Liu, C. Zhou, X. Ren, Recent progress on BaTiO3-based piezoelectric ceramics for actuator applications, Actuators 6 (2017) 24.

[3] T. Zheng, J. Wu, D. Xiao, J. Zhu, Recent development in lead-free perovskite piezoelectric bulk materials, Prog. Mater. Sci. 98 (2018) 552–624.

[4] W. Liu, X. Ren, Large piezoelectric effect in Pb-free ceramics, Phys. Rev. Lett. 103 (2009), 257602.

[5] D. Xue, Y. Zhou, H. Bao, C. Zhou, J. Gao, X. Ren, Elastic, piezoelectric, and dielectric properties of Ba(Zr0.2Ti0.8)O3-(Ba0.7Ca0.3)TiO3 Pb-free ceramic at the morphotropic phase boundary, J. Appl. Phys. 109 (2011), 054110.

[6] Y. Zhang, H. Sun, W. Chen, A brief review of Ba(Ti0.8Zr0.2)O3-(Ba0.7Ca0.3)TiO3 based lead-free piezoelectric ceramics: past, present and future perspectives, J. Phys. Chem. Solids 114 (2018) 207–219.

[7] A. Blazquez-Castro, A. Garcia-Cabañes, M. Carrascosa, Biological applications of ferroelectric materials, Appl. Phys. Rev. 5 (2018), 041101.

[8] T.E. Hooper, J.I. Roscow, A. Mathieson, H. Khanbareh, A.J. Goetzee-Barral, A. J. Bell, High voltage coefficient piezoelectric materials and their applications, J. Eur. Ceram. Soc. 41 (2021) 6115–6129.

[9] T. Zheng, J. Wu, D. Xiao, J. Zhu, Recent development in lead-free perovskite piezoelectric bulk materials, Prog. Mater. Sci. 98 (2018) 552–624.

[10] I. Coondoo, N. Panwar, H. Amorín, M. Algueró, A.L. Kholkin, Synthesis and characterization of lead-free 0.5Ba(Zr0.2Ti0.8)O3-0.5(Ba0.7Ca0.3)TiO3 ceramic, J. Appl. Phys. 113 (2013), 214107.

[11] Y. Huang, C. Zhao, B. Wu, X. Zhang, Grain size effects and structure origin in high performance BaTiO3-based piezoceramics with large grains, J. Eur. Ceram. Soc. 42 (2022) 2764–2771.

[12] H. Amorín, M. Venet, E. Chinarro, P. Ramos, M. Algueró, Alicia Castro, Lead-free Ba0.85Ca0.15Zr0.1Ti0.9O3 ferroelectric ceramics with refined microstructure and high strain under electric field by mechanosynthesis, J. Eur. Ceram. Soc. 42 (2022) 4907–4916.

[13] J. Rödel, K.G. Webber, R. Dittmer, W. Jo, M. Kimura, D. Damjanovic, Transferring lead-free piezoelectric ceramics into application, J. Eur. Ceram. Soc. 35 (2015) 1659–1681.

[14] J. Koruza, A.J. Bell, T. Fromling, K.G. Webber, K. Wang, J. Rödel, Requirements for the transfer of lead-free piezoceramics into application, J. Mater. 4 (2018) 13–26.

[15] J. Hao, W. Bai, W. Li, J. Zhai, Correlation between the microstructure and electrical properties in high-performance (Ba0.85Ca0.15)(Zr0.1Ti0.9)O3 lead-free piezoelectric ceramics, J. Am. Ceram. Soc. 95 (2012) 1998–2006.

[16] F. Benabdallah, C. Elissalde, U.C.C. Seu, D. Michau, A. Poulon-Quintin, M. Gayot, P. Garreta, H. Khemakhem, M. Maglione, Structure-microstructure-property relationships in lead-free BCTZ piezoceramics processed by conventional sintering and spark plasma sintering, J. Eur. Ceram. Soc. 35 (2015) 4153–4161.

[17] V. Bijalwan, V. Prajzler, J. Erhart, H. Tan, P. Roupcova, D. Sobola, P. Tofel, K. Maca, Rapid pressure-less and spark plasma sintering of (Ba0.85Ca0.15Zr0.1Ti0.9) O3 lead-free piezoelectric ceramics, J. Eur. Ceram. Soc. 41 (2021) 2514–2523.

[18] M. Cologna, B. Rashkova, R. Raj, Flash sintering of nanograin zirconia in< 5 s at 850C, J. Am. Ceram. Soc. 93 (2010) 3556–3559.

[19] C.E.J. Dancer, Flash sintering of ceramic materials, Mater. Res. Express 3 (2016), 102001.

[20] M. Biesuz, V.M. Sglavo, Flash sintering of ceramics, J. Eur. Ceram. Soc. 39 (2019) 115–143.

[21] P. Kumar MK, D. Yadav, J.-M. Lebrun, R. Raj, Flash sintering with current rate: a different approach, J. Am. Ceram. Soc. 102 (2019) 823–835.

[22] S. López-Blanco, D.A. Ochoa, X. Vendrell, L. Mestres, J.E. García, Tailoring the microstructure by a proper electric current control in flash sintering: the case of barium titanate, J. Eur. Ceram. Soc. 42 (2022) 5669–5674.

[23] I.R. Lavagnini, J.V. Campos, J.A. Ferreira, E.M.J.A. Pallone, Microstructural evolution of 3YSZ flash-sintered with current ramp control, J. Am. Ceram. Soc. 103 (2020) 3493–3499.

[24] H. Charalambous, S.K. Jha, K.H. Christian, R.T. Lay, T. Tsakalakos, Flash sintering using controlled current ramp, J. Eur. Ceram. Soc. 38 (2018) 3689–3693.

[25] J.E. García, R. Perez, A. Albareda, High electric field measurement of dielectric constant and losses of ferroelectric ceramics, J. Phys. D. Appl. Phys. 34 (2001) 3279.

[26] H. Zhou, X. Li, Y. Zhu, J. Liu, A. Wu, G. Ma, X. Wang, Z. Jia, L. Wang, Review of flash sintering with strong electric field, High. Volt. 7 (2022) 1–11.

[27] I. Coondoo, N. Panwar, D. Alikin, I. Bdikin, S.S. Islam, A. Turygin, V.Y. Shur, A. L. Kholkin, A comparative study of structural and electrical properties in lead-free BCZT ceramics: influence of the synthesis method, Acta Mater. 155 (2018) 331–342.

[28] Y. Tan, J. Zhang, Y. Wu, C. Wang, V. Koval, B. Shi, H. Ye, R. McKinnon, G. Viola, H. Yan, Unfolding grain size effects in barium titanate ferroelectric ceramics, Sci. Rep. 5 (2015) 9953.

[29] A.B. Haugen, J.S. Forrester, D. Damjanovic, B. Li, K.J. Bowman, J.L. Jones, Structure and phase transitions in 0.5(Ba0.7Ca0.3TiO3) −0.5(BaZr0.2Ti0.8O3) from −100 ºC to 150 ºC, J. Appl. Phys. 113 (2013), 014103.

[30] D.S. Keeble, F. Benabdallah, P.A. Thomas, M. Maglione, J. Kreisel, Revised structural phase diagram of (Ba0.7Ca0.3TiO3)-(BaZr0.2Ti0.8O3), Appl. Phys. Lett. 102 (2013), 092903.

[31] A. Manjón-Sanz, C.M. Culbertson, D. Hou, J.L. Jones, M.R. Dolgos, Total scattering and diffraction studies of lead-free piezoelectric (1-x)Ba(Zr0.2Ti0.8)O3-x(Ba0.7Ca0.3) TiO3 deconvolute intrinsic and extrinsic contributions to electromechanical strain, Acta Mater. 171 (2019) 79–91.

[32] H. Liu, J. Chen, H. Huang, L. Fan, Y. Ren, Z. Pan, J. Deng, L.-Q. Chen, X. Xing, Role of reversible phase transformation for strong piezoelectric performance at the morphotropic phase boundary, Phys. Rev. Lett. 120 (2018), 055501.

[33] D.A. Ochoa, A. Reyes-Montero, M.E. Villafuerte-Castrejón, L. Pardo, E. Jose Garcia, Assessment of the functional properties stability in (Ba0.85Ca0.15) (Zr0.1Ti0.9)O3 piezoceramics: huge dielectric and piezoelectric nonlinearity, J. Alloy. Comp. 774 (2019) 410–417.

[34] J. Gao, X. Hu, L. Zhang, F. Li, L. Zhang, Y. Wang, Y. Hao, L. Zhong, X. Ren, Major contributor to the large piezoelectric response in (1–x)Ba(Zr0.2Ti0.8)O3–x (Ba0.7Ca0.3)TiO3 ceramics: domain wall motion, Appl. Phys. Lett. 104 (2014), 252909.

[35] D. Damjanovic, M. Demartin, The Rayleigh law in piezoelectric ceramics, J. Phys. D. Appl. Phys. 29 (1999) 2057–2060.

[36] D.A. Hall, Nonlinearity in piezoelectric ceramics, J. Mater. Sci. 36 (2001) 4575.

[37] J.E. García, R. Pérez, D.A. Ochoa, A. Albareda, M.H. Lente, J.A. Eiras, Evaluation of domain wall motion in lead zirconate titanate ceramics by nonlinear response measurements, J. Appl. Phys. 103 (2008) 054108.

[38] D.A. Ochoa, F. Suñol, F. Rubio-Marcos, J.E. García, Enhancement of piezoelectric properties stability of submicron-structured piezoceramics obtained by spark plasma sintering, J. Eur. Ceram. Soc. 38 (2018) 4659–4663.